Am J Transl Res 2026;18(4):2999-3014
www.ajtr.org /ISSN:1943-8141/AJTR0171295

Original Article

Construction and validation of a predictive model for drug resistance in clear cell renal cell carcinoma based on the heterogeneous characteristics of pathological omics

Guangchi Xu[1], Yin Meng[1], Yongfeng Cui[2], Ji Li[1], Pucheng Yang[1], Wenyu Wang[1], Songtao Liu[1]

[1]Department of Urology, The Second Affiliated Hospital of Qiqihar Medical University, Qiqihar 161006, Heilongjiang, China; [2]Department of Urology, Beitun Hospital of The 10th Division of Xinjiang Production and Construction Corps, Beitun 836099, Xinjiang Uygur Autonomous Region, China

Received January 7, 2026; Accepted March 27, 2026; Epub April 15, 2026; Published April 30, 2026

Abstract: *Objectives:* Therapeutic resistance in advanced clear cell renal cell carcinoma (ccRCC) is partly driven by intra-tumoral heterogeneity. This study aimed to develop and validate a predictive model for drug resistance by integrating pathomic heterogeneity features from histopathologic images with clinical variables. *Methods:* This retrospective study included 358 patients from The Cancer Genome Atlas (TCGA)-KIRC (training cohort) and 143 patients from an independent hospital cohort (2018-2022) for external validation. Resistance was defined as radiological progression within 12 months of starting first-line VEGFR-TKI therapy. Whole-slide images were processed to extract pathomics features: nuclear morphometry (area, perimeter, eccentricity) and texture features (contrast, correlation, energy, homogeneity), with standard deviations quantifying heterogeneity. Nuclear Heterogeneity Proportion (NHP) was calculated as the percentage of patches with significant nuclear heterogeneity. A predictive model combining significant pathomics and clinical features was constructed using multivariate logistic regression and presented as a nomogram. *Results:* The resistant group (n=162) showed significantly higher NHP (39.72% vs. 26.84%, $P<0.001$) and greater heterogeneity in all nuclear and textural features versus non-resistant group (n=196). Multivariate analysis identified high NHP (OR=10.885, $P<0.001$), large tumor size (OR=2.897, $P=0.002$), advanced TNM stage (OR=2.814, $P=0.015$), metastasis (OR=2.642, $P=0.029$), and older age (OR=2.624, $P=0.021$) as independent predictors. The integrated model achieved an AUC of 0.888 internally and 0.925 upon external validation, with 0.897 sensitivity and 0.875 specificity. *Conclusions:* The integrated pathomic-clinical model robustly predicts drug resistance in ccRCC, highlighting the value of computational pathology for risk stratification and personalized treatment planning.

Keywords: Clear cell renal cell carcinoma, pathological omics, drug resistance mechanism

Introduction

Clear cell renal cell carcinoma (ccRCC) represents the most prevalent histologic subtype of renal cancer, accounting for 70-75% of cases, and its incidence has been steadily increasing globally. While early diagnosis rates have improved, advanced ccRCC remains [1] a formidable clinical challenge due to its high propensity for metastasis and development of therapeutic resistance [1, 2]. The current management of metastatic ccRCC relies on a combination of anti-angiogenic agents, mTOR inhibitors, and immunotherapeutic drugs [2, 3]. Despite these advances, the efficacy of these therapies is often limited, and a significant proportion of patients inevitably develop resistance, leading to disease progression [2, 3].

The mechanisms underlying drug resistance in ccRCC are complex and multifactorial. Resistance is not merely a static failure but often a dynamic, reversible process of tumor adaptation [4]. Key mechanisms include epithelial-mesenchymal transition (EMT), which confers a more aggressive and mobile phenotype to cancer cells, the emergence of cancer stem cells (CSCs) that drive tumor regeneration, and

https://doi.org/10.62347/PQIM3135

angiogenic escape by the activation of alternative survival pathways that bypass targeted therapy [4]. This heterogeneity in resistance mechanisms underscores the limitations of current single-target approaches and highlights the need for strategies that can address the multifaceted nature of the problem [2].

A critical factor complicating treatment is the profound intra-tumor heterogeneity inherent to ccRCC [5, 6]. Genetic and molecular diversity exists not only between different patients' tumors but also within different regions of a single tumor [7]. Multiregional sequencing studies have revealed that while driver mutations like VHL are ubiquitous, mutations in genes such as SETD2, PBRM1, and MTOR can be heterogeneous, contributing to varied clonal populations with differing drug sensitivities [7, 8]. This heterogeneity is a significant driver of metastasis, recurrence, and ultimately, therapeutic failure [6].

The integration of multi-omics data, encompassing genomic, transcriptomic, and proteomic layers, provides a powerful framework for deciphering this complexity [9, 10]. Furthermore, histopathologic images, a routine component of clinical diagnosis, contain a wealth of underutilized information. Recent advances in artificial intelligence have demonstrated that deep learning models can extract predictive features from these images to forecast molecular genetics, prognosis, and response to therapy [11, 12]. This approach leverages existing clinical resources to uncover biological insights non-invasively.

Therefore, there is a compelling need to develop predictive frameworks that comprehensively capture and quantify pathologic heterogeneity. By integrating multi-dimensional features derived from pathological omics, such a model could more accurately reflect the complex biological state of the tumor and its microenvironment. This approach will capture intricate interactions within the tumor microenvironment, leading to personalized medicine and improved outcome for patients with ccRCC.

Patients and methods

Patient cohort and data collection

A retrospective study was conducted using two independent cohorts for model development and external validation. The training cohort comprised 358 patients with clear cell renal cell carcinoma (ccRCC) from The Cancer Genome Atlas Kidney Renal Clear Cell Carcinoma (TCGA-KIRC) project. Inclusion criteria were: (1) histopathologically confirmed ccRCC; (2) availability of high-quality hematoxylin and eosin (H&E)-stained whole slide images (WSIs); (3) availability of essential clinical data, including age, gender, tumor stage (AJCC 8th edition TNM staging), Fuhrman nuclear grade, and overall survival (OS) follow-up information; and (4) treatment with first-line VEGFR-TKI monotherapy (sunitinib or pazopanib). Patients who received immune checkpoint inhibitors or combination therapies were excluded to avoid treatment confounding. Based on treatment response evaluation, the training cohort included 196 patients in the non-resistant group and 162 in the resistant group.

An independent test cohort consisted of 143 patients diagnosed with ccRCC at Hospital between January 2018 and June 2022, from whom 230 formalin-fixed paraffin-embedded (FFPE) tissue blocks were collected. The same inclusion criteria were applied, resulting in 40 non-resistant and 29 resistant patients.

In both cohorts, resistance was defined as radiological disease progression within 12 months of initiating first-line systemic therapy (sunitinib or pazopanib), according to RECIST version 1.1. This definition captures clinically relevant early treatment failure, encompassing both primary resistance (progression as best response) and early acquired resistance (progression after initial response or stable disease <12 months). The non-resistant group included patients with partial response, complete response, or stable disease for at least 12 months [13]. One experienced pathologist independently reviewed and annotated WSIs from the test cohort using the Automated Slide Analysis Platform (ASAP) version 1.9 to delineate tumor and non-tumor regions of interest (ROIs).

This retrospective study was conducted in accordance with the ethical standards of the The Second Affiliated Hospital of Qiqihar Medical University institutional and national research committees and with the 1964 Helsinki declaration and its later amendments. The training cohort data were obtained from TCGA-KIRC project. Since the data are de-identified and

publicly available, additional institutional review board approval was not required for the training cohort analysis. For the independent hospital test cohort, the study protocol was reviewed and approved by the Institutional Review Board of The Second Affiliated Hospital of Qiqihar Medical University. Due to the retrospective nature of this study, which involved the analysis of existing archival FFPE tissue blocks and de-identified clinical data collected during routine clinical care, the requirement for written informed consent from patients was waived by the The Second Affiliated Hospital of Qiqihar Medical University Institutional Review Board. All patient data were fully anonymized prior to analysis to protect patient confidentiality.

WSI preprocessing and tumor region segmentation

Digital WSIs from both the TCGA training cohort and the hospital test cohort underwent a systematic preprocessing pipeline to facilitate computational analysis. The WSIs were initially processed using the Open Source Computer Vision Library (OpenCV) version 4.5.5 to automatically identify and remove non-informative background areas, specifically white regions with RGB values exceeding 240 on a 0-255 scale. Following background removal, the remaining tissue areas were processed to address technical variations in staining intensity and color. Color normalization was performed using the StainTools Python toolkit version 0.2.0 and PathML toolkit version 0.1.5. These tools leverage stain decomposition algorithms, specifically the Macenko algorithm, to separate the H&E stain vectors and normalize the color appearance of all WSIs to a reference stain matrix. Data augmentation techniques were applied to the extracted image patches, including random 90° and 180° rotations, random horizontal and vertical flipping, and image shifts of up to 10% of the patch dimensions. The entire WSI was segmented into smaller image patches of 300×300 pixels using the OpenSlide library version 3.4.1. From these patches, those containing viable tumor tissue were selected based on pathologist annotations for the test cohort and corresponding tumor regions identified in TCGA metadata for the training cohort. Positive patches were defined as those exhibiting marked variation in nuclear size (coefficient of variation >0.3), shape (eccentricity >0.7 in >20% of nuclei), and chromatin pattern. These thresholds were selected based on prior studies linking high nuclear pleomorphism (CV >0.3) to genomic instability and poor prognosis [14], and eccentricity >0.7 to mesenchymal-like morphology associated with invasive potential [14]. Negative patches showed relatively uniform nuclei with variation coefficient <0.2 and eccentricity <0.5 in >80% of nuclei, representing low-heterogeneity regions [14].

Pathomics feature extraction and heterogeneity quantification

The pathomic analysis involved quantitative extraction of features from nuclear morphology and tissue texture within tumor ROIs. An automated pipeline for nuclear segmentation and feature extraction was constructed using CellProfiler version 4.2.1. The pipeline identified individual cell nuclei through a combination of color deconvolution using the Haematoxylin-Eosin-DAB (HED) color space and Otsu's thresholding-based segmentation. For each segmented nucleus, morphometric features were calculated: Area (measured in square micrometers), Perimeter (measured in micrometers), and Eccentricity (dimensionless ratio from 0 to 1). Textural features were extracted from the grayscale version of the image patch within a perinuclear region of 50×50 pixels centered on each nucleus. These texture features, derived from a Gray-Level Co-Occurrence Matrix (GLCM) with a distance of 1 pixel and angles of 0°, 45°, 90°, and 135°, included: Contrast (measuring local intensity variations), Correlation (measuring linear dependencies of gray levels), Energy (measuring textural uniformity), and Homogeneity (measuring the closeness of GLCM element distribution to the diagonal). To capture intra-tumoral heterogeneity while avoiding the pitfalls of high-dimensional data, we aggregated patch-level measurements for each patient by calculating the SD of each nuclear and texture feature across all tumor patches from that patient's WSI. This approach condenses the distribution of each feature into a single interpretable metric reflecting variability, thereby reducing dimensionality and mitigating multicollinearity. The Nuclear Heterogeneity Proportion (NHP) was calculated as the percentage of image patches classified as positive for nuclear heterogeneity relative to the total number of tumor patches analyzed per patient. Consequently, only 8 pathomics heterogeneity features (7 SDs + NHP) were used as candidate

predictors in the logistic regression model, not the thousands of raw patch-level measurements.

Construction and validation of a drug resistance prediction model

The prediction model for drug resistance was constructed using the TCGA training cohort by integrating pathomic heterogeneity features and clinical predictors that were statistically significant in the multivariate logistic regression analysis. These included the NHP, ECOG performance status, TNM stage, Fuhrman grade, and presence of metastasis.

To translate the risk score into a clinically useful binary classifier, the optimal cut-off value was determined by maximizing the Youden index in the receiver operating characteristic (ROC) analysis of the training cohort. This allowed stratification of patients into high-risk and low-risk groups. The model's discriminative ability was quantified by the area under the ROC curve (AUC). The fully specified model was then locked and applied without any retraining, parameter adjustment, or additional multivariable analysis to the independent hospital test cohort. Risk scores were calculated for each patient in the test set using the established regression coefficients, and the same pre-defined cut-off value was applied for dichotomization. Model performance was evaluated on this external cohort solely by computing the AUC, sensitivity, and specificity to assess discriminative ability, without performing any new multivariate fitting.

Statistical analysis

All statistical analyses were conducted using SPSS version 19.0 and R version 3.0.2 with the 'survival', 'rms', and 'dcurves' packages. For model development in the training cohort, the events-per-variable (EPV) ratio was calculated to assess statistical power; an EPV ≥10 was considered adequate for multivariate logistic regression. For the external validation cohort, as the pre-locked model was applied without refitting, a formal sample size calculation was not required. Normality of continuous variables was assessed using the Shapiro-Wilk test. Normally distributed variables were expressed as mean ± standard deviation and compared using unpaired t-tests; non-normal variables were summarized as median with interquartile range and compared using the Mann-Whitney U test. Categorical variables were reported as frequencies and percentages and compared by chi-square or Fisher's exact test, as appropriate. Univariate and multivariate logistic regression models were applied to identify predictors of drug resistance, with results reported as odds ratios (OR) and 95% confidence intervals (CI). Model calibration was assessed using the Hosmer-Lemeshow goodness-of-fit test, the Brier score (a measure of the mean squared difference between predicted probabilities and observed outcomes, ranging from 0 to 1, with lower values indicating better calibration), and the calibration slope (ideal value =1). Decision curve analysis (DCA) was performed to evaluate clinical net benefit across a range of threshold probabilities. All tests were two-sided, with $P<0.05$ considered significant. The training and test cohorts were analyzed separately to maintain validation integrity.

Results

Baseline clinical and demographic characteristics of the training cohort

In the training cohort, significant differences were observed between the resistant and non-resistant groups for several baseline characteristics (**Table 1**). The resistant group was older (64.78 ± 9.12 years vs. 62.34 ± 8.67 years, $P=0.010$), had a higher proportion of smokers (50.62% vs. 39.80%, $P=0.040$), and a worse ECOG performance status (35.80% with PS=1 vs. 23.47%, $P=0.011$). No significant differences were found in BMI, gender, marital status, race, drinking history, hypertension, diabetes, or valvular heart disease (all $P>0.05$). Regarding disease-related characteristics (**Table 2**), the resistant group had larger tumor size (6.73 ± 1.89 cm vs. 5.54 ± 1.42 cm, $P<0.001$), more advanced TNM stage (e.g., 25.93% Stage III vs. 14.80%, $P=0.003$), higher Fuhrman grade (e.g., 29.63% Grade 3 vs. 19.90%, $P=0.033$), and a greater presence of metastasis (23.46% vs. 12.76%, $P=0.008$). Treatment regimen and laterality did not differ significantly between groups.

Comparison of pathomics heterogeneity features between resistant and non-resistant groups in the training cohort

Significant differences in pathomics heterogeneity features were evident between the resis-

Table 1. Baseline characteristics of patients in the training cohort

Item	Non-resistant group (n=196)	Resistant group (n=162)	t/χ^2	*P* value
Age (years)	62.34 ± 8.67	64.78 ± 9.12	2.596	0.010
BMI (kg/m^2)	28.51 ± 4.23	29.07 ± 4.16	1.244	0.214
Gender [n (%)]			1.012	0.314
Male	137 (69.90%)	121 (74.69%)		
Female	59 (30.10%)	41 (25.31%)		
Marital Status [n (%)]			0.301	0.860
Married	142 (72.45%)	114 (70.37%)		
Single	32 (16.33%)	30 (18.52%)		
Divorced	22 (11.22%)	18 (11.11%)		
Race [n (%)]			0.436	0.509
Asian	179 (91.33%)	151 (93.21%)		
Other	17 (8.67%)	11 (6.79%)		
Smoking history [n (%)]			4.202	0.040
Yes	78 (39.80%)	82 (50.62%)		
No	118 (60.20%)	80 (49.38%)		
Drinking history [n (%)]			0.517	0.472
Yes	69 (35.20%)	63 (38.89%)		
No	127 (64.80%)	99 (61.11%)		
Hypertension [n (%)]			0.122	0.727
Yes	98 (50.00%)	84 (51.85%)		
No	98 (50.00%)	78 (48.15%)		
Diabetes [n (%)]			0.001	0.973
Yes	39 (19.90%)	32 (19.75%)		
No	157 (80.10%)	130 (80.25%)		
Valvular Heart Disease [n (%)]			0.036	0.849
Yes	10 (5.10%)	9 (5.56%)		
No	186 (94.90%)	153 (94.44%)		
ECOG PS [n (%)]			6.545	0.011
0	150 (76.53%)	104 (64.20%)		
1	46 (23.47%)	58 (35.80%)		

Note: BMI, body mass index; ECOG PS, Eastern Cooperative Oncology Group Performance Status.

tant and non-resistant groups in the training cohort (**Figure 1**). The resistant group exhibited higher SD for nuclear area (14.47 ± 4.12 μm^2 vs. 12.33 ± 3.21 μm^2, *P*<0.001), nuclear perimeter (11.23 ± 2.89 μm vs. 9.76 ± 2.34 μm, *P*< 0.001), nuclear eccentricity (0.14 ± 0.04 vs. 0.12 ± 0.04, *P*<0.001), and texture contrast (29.12 ± 7.45 vs. 26.43 ± 6.78, *P*<0.001). Conversely, the resistant group showed significantly lower values for SD of texture correlation (0.39 ± 0.11 vs. 0.43 ± 0.12, *P*=0.002), SD of texture energy (0.19 ± 0.05 vs. 0.22 ± 0.06, *P*<0.001), and SD of texture homogeneity (0.61 ± 0.16 vs. 0.67 ± 0.18, *P*<0.001). Most notably, the Nuclear Heterogeneity Proportion (NHP) was substantially higher in the resistant group (39.72 ± 10.84% vs. 26.84 ± 9.12%, *P*<0.001).

Univariate and multivariate logistic regression analyses for predicting drug resistance

Univariate logistic regression identified several clinical and dichotomized pathomics features significantly associated with drug resistance, including age ≥55.94 years (OR=2.192, *P*= 0.004), smoking history (OR=1.551, *P*=0.041), ECOG PS ≥1 (OR=1.819, *P*=0.011), tumor size ≥6.515 cm (OR=3.854, *P*<0.001), TNM stage ≥II (OR=1.990, *P*=0.001), Fuhrman grade ≥3 (OR=1.860, *P*=0.007), presence of metastasis (OR=2.096, *P*=0.009), and high values (above optimal cut-off) for all pathomics heterogeneity features (all *P*<0.001), with NHP ≥32.735% showing the strongest association (OR=9.100, *P*<0.001) (**Table 3**). In the multivariate analysis,

Table 2. Disease-related clinical characteristics in the training cohort

Item	Non-resistant group (n=196)	Resistant group (n=162)	t/χ^2	*P* value
Treatment Regimen [n (%)]			0.236	0.627
Sunitinib	99 (50.51%)	86 (53.09%)		
Pazopanib	97 (49.49%)	76 (46.91%)		
Tumor size (cm)	5.54 ± 1.42	6.73 ± 1.89	6.628	<0.001
TNM stage [n (%)]			14.164	0.003
Stage I	112 (57.14%)	65 (40.12%)		
Stage II	45 (22.96%)	38 (23.46%)		
Stage III	29 (14.80%)	42 (25.93%)		
Stage IV	10 (5.10%)	17 (10.49%)		
Fuhrman grade [n (%)]			8.768	0.033
Grade 1	58 (29.59%)	32 (19.75%)		
Grade 2	89 (45.41%)	68 (41.98%)		
Grade 3	39 (19.90%)	48 (29.63%)		
Grade 4	10 (5.10%)	14 (8.64%)		
Laterality [n (%)]			0.039	0.844
Left	102 (52.04%)	86 (53.09%)		
Right	94 (47.96%)	76 (46.91%)		
Presence of metastasis [n (%)]			7.005	0.008
Yes	25 (12.76%)	38 (23.46%)		
No	171 (87.24%)	124 (76.54%)		

Note: TNM, Tumor Node Metastasis.

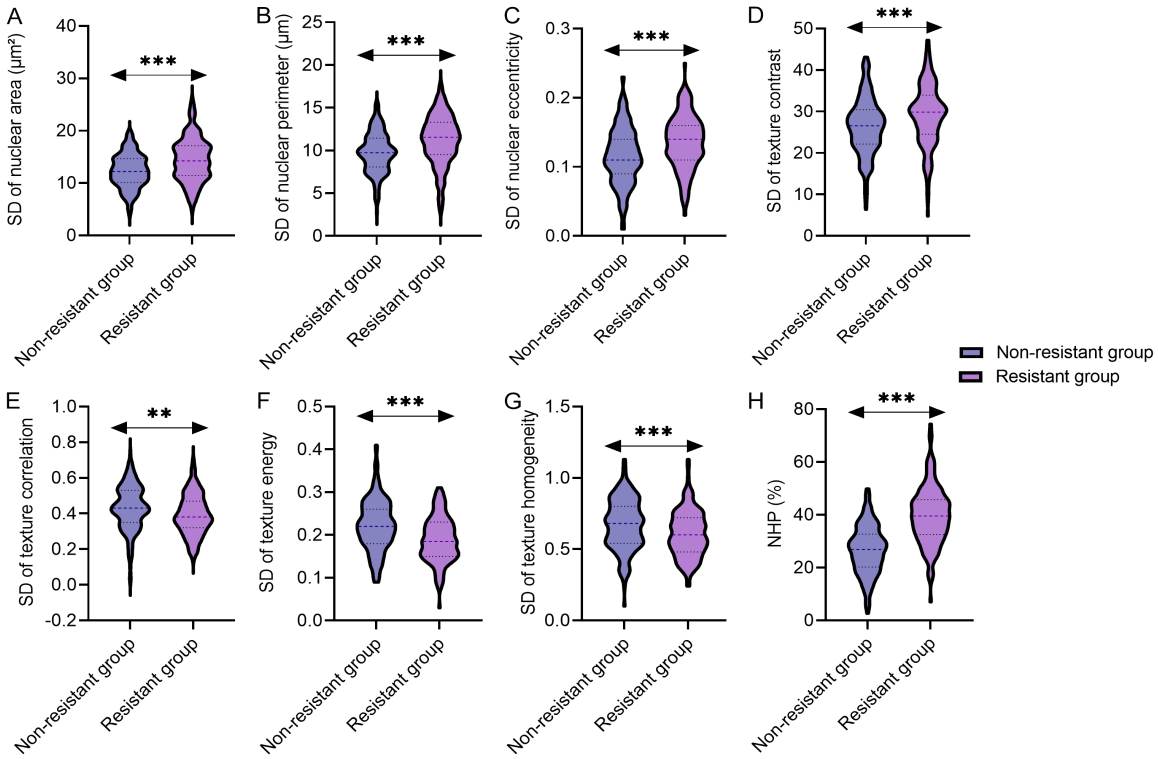

Figure 1. Comparison of pathomic heterogeneity features in the training cohort. A. SD of nuclear area; B. SD of nuclear perimeter; C. SD of nuclear eccentricity; D. SD of texture contrast; E. SD of texture correlation; F. SD of texture energy; G. SD of texture homogeneity; H. NHP. Note: SD: Standard Deviation; NHP: Nuclear Heterogeneity Proportion. **P<0.01; ***P<0.001.

Table 3. Univariate and multivariate logistic regression analyses of clinical and pathomics features for drug resistance

Variable	Univariate Logistic analysis		Multivariate Logistic analysis	
	OR	*P* value	OR	*P* value
Age (≥55.94 years)	2.192 (1.307-3.762)	0.004	2.624 (1.155-5.961)	0.021
Smoking history (Yes)	1.551 (1.020-2.365)	0.041	0.844 (0.446-1.595)	0.601
ECOG PS (≥1)	1.819 (1.149-2.893)	0.011	0.668 (0.076-5.849)	0.715
Tumor size (≥6.515 cm)	3.854 (2.471-6.079)	<0.001	2.897 (1.495-5.615)	0.002
TNM stage (≥II)	1.990 (1.307-3.046)	0.001	2.814 (1.225-6.461)	0.015
Fuhrman grade (≥3)	1.860 (1.185-2.934)	0.007	1.666 (0.190-14.612)	0.645
Metastasis (Yes)	2.096 (1.210-3.687)	0.009	2.642 (1.102-6.377)	0.029
SD nuclear area (≥15.455 μm^2)	3.959 (2.414-6.626)	<0.001	5.579 (2.557-12.176)	<0.001
SD nuclear perimeter (≥10.395 μm)	3.484 (2.261-5.421)	<0.001	2.826 (1.492-5.352)	0.001
SD nuclear eccentricity (≥0.115)	2.708 (1.747-4.245)	<0.001	2.723 (1.412-5.252)	0.003
SD texture contrast (≥29.125)	2.706 (1.763-4.183)	<0.001	3.971 (2.035-7.751)	<0.001
SD texture correlation (≥0.385)	0.400 (0.258-0.616)	<0.001	0.472 (0.250-0.890)	0.020
SD texture energy (≥0.195)	0.343 (0.222-0.528)	<0.001	0.364 (0.191-0.692)	0.002
SD texture homogeneity (≥0.675)	0.432 (0.279-0.665)	<0.001	0.490 (0.254-0.943)	0.033
NHP (≥32.735%)	9.100 (5.676-14.875)	<0.001	10.885 (5.540-21.385)	<0.001

Note: ECOG PS, Eastern Cooperative Oncology Group Performance Status; TNM, Tumor Node Metastasis; SD, Standard Deviation; NHP, Nuclear Heterogeneity Proportion.

the following variables retained independent significance: age ≥55.94 years (OR=2.624, *P*=0.021), tumor size ≥6.515 cm (OR=2.897, *P*=0.002), TNM stage ≥II (OR=2.814, *P*=0.015), presence of metastasis (OR=2.642, *P*=0.029), and high values for all individual pathomic heterogeneity features: SD of nuclear area (OR=5.579, *P*<0.001), SD of nuclear perimeter (OR=2.826, *P*=0.001), SD of nuclear eccentricity (OR=2.723, *P*=0.003), SD of texture contrast (OR=3.971, *P*<0.001), SD of texture correlation (OR=0.472, *P*=0.020), SD of texture energy (OR=0.364, *P*=0.002), SD of texture homogeneity (OR=0.490, *P*=0.033), and NHP (OR=10.885, *P*<0.001). Conversely, smoking history, ECOG PS, and Fuhrman grade did not retain independent significance in the multivariate model (all *P*≥0.05).

Receiver operating characteristic (ROC) analysis of individual pathomics features for predicting drug resistance

ROC analysis of pathomics features for discriminating drug resistance revealed several key findings. The SD of nuclear area with a best threshold of 15.455 μm^2 had a sensitivity of 0.407, specificity of 0.852, and an AUC of 0.65 (Youden index =0.259; F1 score =0.624) (**Table 4**). For the SD of nuclear perimeter at a threshold of 10.395 μm, the sensitivity was 0.654, specificity 0.648, and the AUC reached 0.668 (Youden index =0.302; F1 score =0.509). The SD of nuclear eccentricity showed a sensitivity of 0.722, specificity of 0.510, and an AUC of 0.644 (Youden index =0.232; F1 score =0.436), whereas the SD of texture contrast, with a best threshold of 29.125, had a sensitivity of 0.562, specificity of 0.679, and an AUC of 0.619 (Youden index =0.241; F1 score =0.600). The SD of texture correlation, at a threshold of 0.385, demonstrated a sensitivity of 0.512, specificity of 0.704, and an AUC of 0.608 (Youden index =0.216; F1 score =0.566). The SD of texture energy, with a best threshold of 0.195, achieved a sensitivity of 0.574, specificity of 0.684, and an AUC of 0.665 (Youden index =0.258; F1 score =0.454). The SD of texture homogeneity, at its optimal threshold of 0.675, resulted in a sensitivity of 0.685, specificity of 0.515, and an AUC of 0.616 (Youden index =0.200; F1 score =0.338). Notably, the NHP with a best threshold of 32.735% exhibited the highest discriminatory power among all features, with a sensitivity of 0.747, specificity of 0.755, and an AUC of 0.822 (Youden index =0.502; F1 score =0.514).

Survival analysis stratified by optimal cut-off values of pathomic features

Kaplan-Meier survival analysis with log-rank testing demonstrated that all eight pathomic heterogeneity features significantly stratified

Table 4. ROC analysis of pathomics features for discriminating drug resistance in the training cohort

Variable	Best threshold	Sensitivities	Specificities	AUC	Youden index	F1 score
SD of nuclear area (μm^2)	15.455	0.407	0.852	0.65	0.259	0.624
SD of nuclear perimeter (μm)	10.395	0.654	0.648	0.668	0.302	0.509
SD of nuclear eccentricity	0.115	0.722	0.510	0.644	0.232	0.436
SD of texture contrast	29.125	0.562	0.679	0.619	0.241	0.600
SD of texture correlation	0.385	0.512	0.704	0.608	0.216	0.566
SD of texture energy	0.195	0.574	0.684	0.665	0.258	0.454
SD of texture homogeneity	0.675	0.685	0.515	0.616	0.200	0.338
NHP (%)	32.735	0.747	0.755	0.822	0.502	0.514

Note: SD, Standard Deviation; NHP, Nuclear Heterogeneity Proportion.

patients into distinct prognostic groups based on their optimal cut-off values (**Figure 2**). Patients classified into the high-heterogeneity groups for SD of nuclear area (OS: 28.43 ± 8.67 vs. 45.67 ± 9.34 months, P<0.001), SD of nuclear perimeter (OS: 29.78 ± 7.84 vs. 44.12 ± 8.91 months, P<0.001), SD of nuclear eccentricity (OS: 30.24 ± 8.23 vs. 43.56 ± 9.12 months, P<0.001), and SD of texture contrast (OS: 31.45 ± 7.98 vs. 42.87 ± 8.76 months, P<0.001) exhibited significantly shorter overall survival. Conversely, for features where a lower value indicates greater disorder, the "High Group" was associated with significantly longer survival, as seen for SD of texture correlation (OS: 41.23 ± 8.45 vs. 32.67 ± 7.89 months, P<0.001), SD of texture energy (OS: 42.34 ± 8.76 vs. 31.56 ± 7.34 months, P< 0.001), and SD of texture homogeneity (OS: 43.12 ± 9.01 vs. 30.89 ± 8.12 months, P< 0.001). Most notably, the Nuclear Heterogeneity Proportion (NHP) showed the most pronounced stratification, with the high-NHP group having a mean OS of only 26.45 ± 7.23 months compared to 46.78 ± 9.67 months in the low-NHP group (P<0.001). These results confirm the strong and consistent prognostic value of intra-tumoral heterogeneity quantified by pathomic features for predicting overall survival in ccRCC patients.

Development and evaluation of the pathomics-based predictive model for drug resistance

A comprehensive predictive model integrating significant pathomic and clinical features was developed and visualized as a nomogram (**Figure 3D**). The model demonstrated excellent calibration, as shown by the close alignment between predicted and observed probabilities in the calibration curve (**Figure 3A**). In the training cohort, the Hosmer-Lemeshow test yielded a non-significant chi-square value of 7.82 (P= 0.441), indicating no significant deviation from perfect fit. The Brier score was 0.112, reflecting good predictive accuracy, and the calibration slope was 0.964 (95% CI: 0.892-1.037), suggesting minimal overfitting. Decision curve analysis (**Figure 3B**) indicated a superior net benefit across a wide range of threshold probabilities, supporting the clinical utility of the model. Furthermore, the clinical impact curve (**Figure 3C**) illustrated the model's ability to accurately identify high-risk patients across different risk thresholds. The combined ROC curve (**Figure 3E**) confirmed the model's strong discriminative performance, with an AUC of 0.888 in the training cohort. These results collectively validate the robustness and potential clinical applicability of the pathomics-based nomogram for predicting drug resistance in ccRCC patients.

External validation of pathomic heterogeneity features in the test cohort

In the external test cohort, all pathomic heterogeneity features remained significantly different between resistant and non-resistant groups (**Table 5**). The resistant group showed higher SD of nuclear area (16.23 ± 4.08 μm^2 vs. 12.87 ± 3.34 μm^2, P<0.001), SD of nuclear perimeter (11.87 ± 2.74 μm vs. 8.94 ± 2.41 μm, P<0.001), and NHP (40.56 ± 10.91% vs. 27.34 ± 9.08%, P<0.001), consistent with the training cohort trends.

Performance of the combined predictive model in the test cohort

The combined predictive model, locked after training, was validated on the independent test cohort, where it maintained outstanding dis-

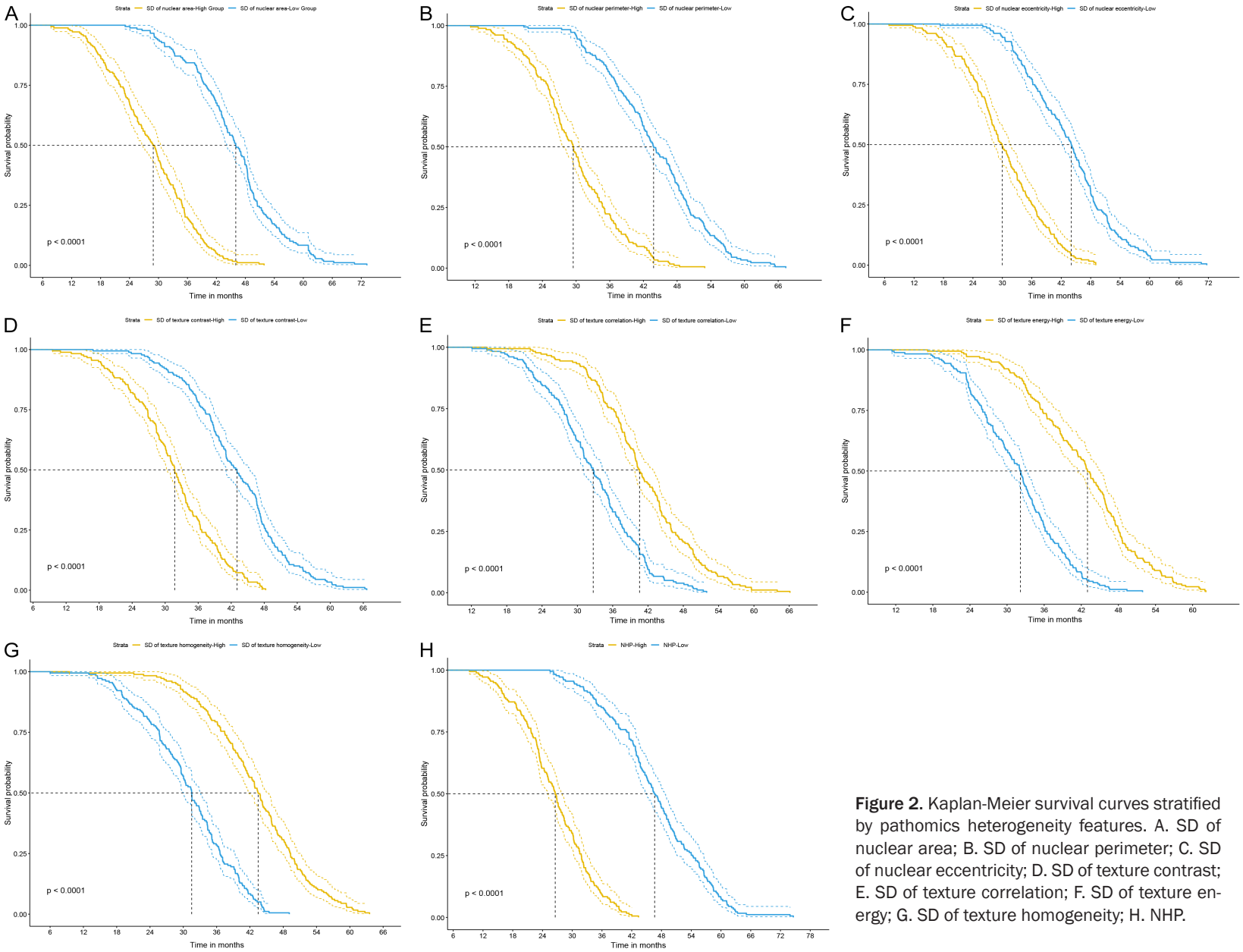

Figure 2. Kaplan-Meier survival curves stratified by pathomics heterogeneity features. A. SD of nuclear area; B. SD of nuclear perimeter; C. SD of nuclear eccentricity; D. SD of texture contrast; E. SD of texture correlation; F. SD of texture energy; G. SD of texture homogeneity; H. NHP.

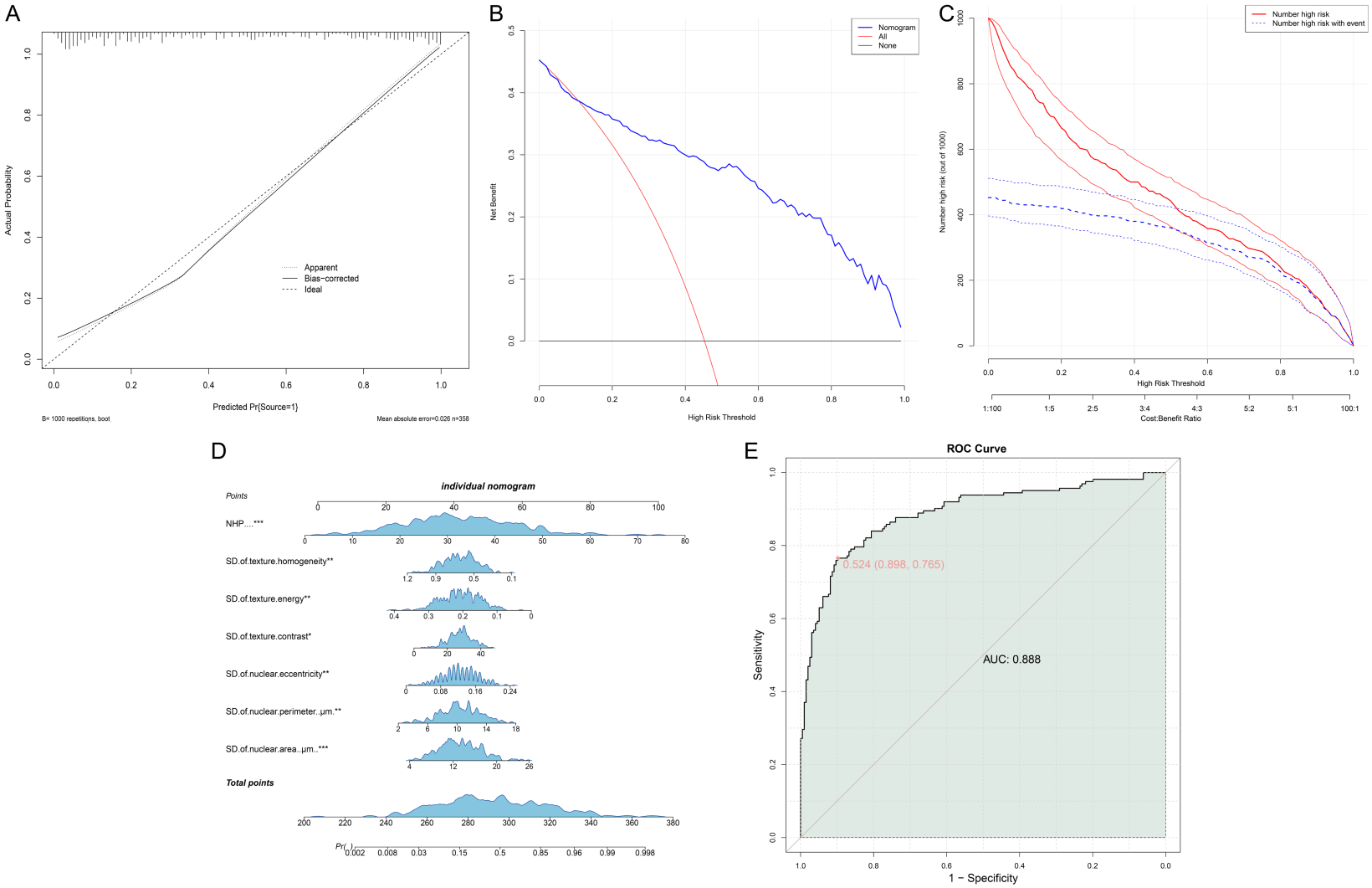

Figure 3. Construction and validation of the nomogram for predicting drug resistance in ccRCC. A. Calibration curve; B. Decision curve analysis; C. Clinical impact curve; D. Nomogram; E. Combined ROC curve.

Table 5. Comparison of pathomics heterogeneity features in the external test cohort

Item	Non-resistant group (n=77)	Resistant group (n=66)	t	*P* value
SD of nuclear area (μm^2)	12.87 ± 3.34	16.23 ± 4.08	5.414	<0.001
SD of nuclear perimeter (μm)	8.94 ± 2.41	11.87 ± 2.74	6.808	<0.001
SD of nuclear eccentricity	0.13 ± 0.04	0.16 ± 0.04	4.357	<0.001
SD of texture contrast	26.12 ± 6.84	29.84 ± 7.23	3.156	0.002
SD of texture correlation	0.46 ± 0.11	0.39 ± 0.10	4.268	<0.001
SD of texture energy	0.24 ± 0.06	0.21 ± 0.05	3.182	0.002
SD of texture homogeneity	0.68 ± 0.17	0.59 ± 0.15	3.350	0.001
NHP (%)	27.34 ± 9.08	40.56 ± 10.91	7.906	<0.001

Note: SD, Standard Deviation; NHP, Nuclear Heterogeneity Proportion.

criminative ability without any refitting (**Figure 4**). Calibration remained robust in the external validation cohort, with a Hosmer-Lemeshow test *P*-value of 0.618, a Brier score of 0.108, and a calibration slope of 0.974 (95% CI: 0.916-1.058). These results confirm the model's excellent calibration and generalizability. The ROC analysis yielded an Area Under the Curve (AUC) of 0.925. This high AUC value, along with a sensitivity of 0.897 and a specificity of 0.875 at the optimal threshold, confirms the model's strong generalizability and reliability for predicting drug resistance in patients with ccRCC.

Discussion

The development of therapeutic resistance remains a major obstacle in the management of advanced clear cell renal cell carcinoma (ccRCC), leading to disease progression and poor outcomes. This study aimed to construct and validate a predictive model for drug resistance in ccRCC by integrating quantitative pathomics heterogeneity features derived from routine histopathological images with established clinical risk factors. Our findings demonstrated that both clinical characteristics and pathomics-based heterogeneity measures are strongly associated with resistance to systemic therapy, and their integration into a comprehensive model provides a robust tool for risk stratification.

The baseline characteristics of our training cohort revealed that patients who developed resistance were generally older, had a higher prevalence of smoking, and exhibited poorer performance status as measured by ECOG scores. These findings align with prior reports, such as those by Mariean et al. [15], who noted that poor performance status and advanced age are often linked to diminished treatment tolerance and increased risk of disease progression. Furthermore, the resistant group presented with more aggressive disease phenotypes, including larger tumor size, advanced TNM stage, higher Fuhrman nuclear grade, and a greater incidence of metastasis. These observations are consistent with the well-established understanding that advanced disease burden correlates with therapeutic challenges, as highlighted in studies such as that by Xiang et al. [16], which described how aggressive tumor biology often underlies acquired resistance mechanisms.

A central finding of this work was the pronounced difference in pathomic heterogeneity features between resistant and non-resistant groups. The resistant group exhibited significantly greater variability in nuclear morphometric features, including nuclear area, perimeter, and eccentricity, indicating heightened nuclear pleomorphism. From a mechanistic standpoint, this morphologic heterogeneity likely stems from underlying genomic instability, a hallmark of ccRCC. The von Hippel-Lindau (VHL) gene is mutated in approximately 80-90% of ccRCC cases, leading to HIF accumulation and activation of downstream pathways promoting angiogenesis, glycolysis, and cell proliferation [1]. However, intra-tumoral heterogeneity is further exacerbated by subclonal mutations in chromatin-modifying genes such as SETD2, PBRM1, and BAP1 [7, 8]. Specifically, SETD2 mutations, which occur in 10-15% of ccRCCs and are often heterogeneous, disrupting H3K36 trimethylation, leading to widespread epigenetic dysregulation, genomic instability, and altered DNA damage repair [5]. This genomic chaos manifests morphologically as increased nuclear size variability (anisokaryosis) and irregular nuclear contours, captured by our SD of nuclear area

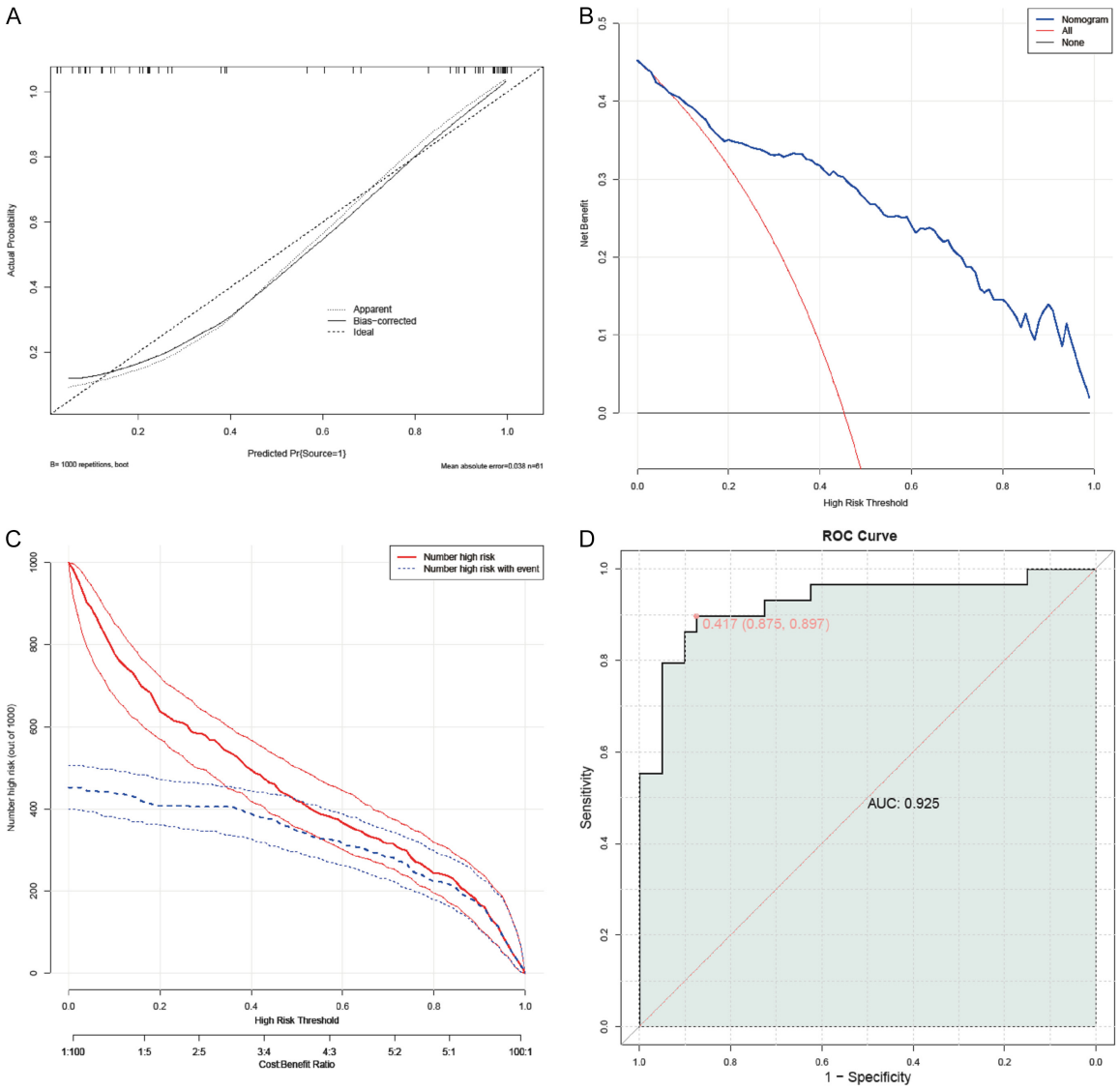

Figure 4. Establishment of combined predictive model in the Test Set. A. Calibration curve; B. Decision curve analysis; C. Clinical impact curve; D. Combined ROC curve.

and perimeter metrics. The strong association of these features with TKI resistance can therefore be interpreted through the lens of clonal diversity: tumors harboring heterogeneous SETD2 (or other driver gene) mutant subclones possess a pre-existing reservoir of cells with differential drug sensitivity, enabling rapid selection of resistant populations under therapeutic pressure [17]. Furthermore, EMT, a program associated with therapeutic escape, is often co-opted in genomically unstable tumors and directly contributes to the nuclear morphologic changes and increased intratumoral diversity we observed [18]. To directly address the mechanistic link between our pathomics features and the underlying genomic landscape, we leveraged the available TCGA data to perform an exploratory correlation analysis. We examined the association between the NHP and the mutation status of key ccRCC driver genes. Patients with SETD2 mutations exhibited significantly higher median NHP scores compared to SETD2-wildtype patients. Similarly, mutations in PBRM1 and BAP1 were also associated with elevated NHP. These findings provide direct evidence that the morphologic heterogeneity quantified by our pathomic pipeline is a surrogate for the presence of disruptive mutations in key chromatin modifier genes. The association with SETD2, in particular, offers a

compelling mechanistic explanation for TKI resistance, as SETD2 loss has been shown to promote resistance through multiple axes: (1) by inducing a pro-angiogenic secretome that sustains tumor vascularization despite VEGFR inhibition [19], and (2) by impairing DNA damage response, leading to the accumulation of further genetic alterations that fuel clonal evolution [5]. Moreover, the textural disorganization captured by our GLCM features (lower correlation, energy, homogeneity) may reflect a disrupted tumor microenvironment, characterized by aberrant tumor vasculature, increased stromal fibrosis, and immune cell exclusion [20]. These microenvironmental barriers compromise uniform drug delivery and create niches that protect resistant clones, thereby contributing to treatment failure. Thus, our pathomics model not only predicts resistance but also captures the integrated phenotypic consequence of key genetic drivers and their downstream effects on the tumor ecosystem.

The univariate and multivariate Logistic regression analyses reinforced the importance of these features, identifying ECOG performance status, TNM stage, Fuhrman grade, presence of metastasis, and NHP as independent predictors of resistance. While clinical factors such as stage and grade have long been recognized as prognostic indicators, the incorporation of NHP adds a novel dimension that captures biological heterogeneity not fully reflected by conventional parameters. This supports the growing consensus, as articulated by Zhang et al. [21], that tumor heterogeneity is a fundamental driver of resistance and progression, necessitating its quantification for accurate risk prediction.

Receiver operating characteristic analysis further underscored the discriminatory power of individual pathomic features, with NHP demonstrating the highest ability to distinguish resistant from non-resistant cases. This finding is consistent with emerging evidence that AI-driven analysis of histopathological images can uncover subtle morphological patterns predictive of molecular phenotypes and treatment outcomes, as demonstrated by Yuan et al. [22] in lymphoid malignancies and Prabhu et al. [23] in solid tumors. The ability of pathomics to extract such information from standard H&E-stained slides offers a practical and non-invasive means to help clinical decision-making.

Survival analysis based on optimal cut-offs for pathomics features revealed that patients classified into high-heterogeneity groups for nuclear morphometry and certain textural features had markedly shorter overall survival. Conversely, for features where lower values indicated greater disorder, the high-value groups were associated with longer survival. This bidirectional relationship highlights the complexity of tumor heterogeneity. While some forms of diversity may indicate adaptive resistance, others may reflect more organized, less aggressive biology [24-26]. The strong stratification achieved by NHP further confirms its value as a integrative biomarker, capturing the net effect of heterogeneous subclones on patient outcomes, as theorized in multi-regional sequencing studies by Gerlinger et al. [17].

The predictive model developed in this study, which combined pathomics and clinical variables, demonstrated high discriminative performance and excellent calibration in both the training and external test cohorts. The model's ability to maintain its accuracy in an independent validation set underscores its generalizability and reliability. Decision curve and clinical impact analyses indicated that the model provides meaningful net benefit across a range of threshold probabilities, supporting its potential utility in clinical settings for identifying high-risk patients who may benefit from alternative treatment strategies or more intensive monitoring. This approach resonates with the call by Steyerberg et al. [27] for the integration of proteomic and morphometric data to advance personalized oncology.

From a mechanistic perspective, the association between pathomic heterogeneity and resistance can be interpreted through several biological pathways. Nuclear morphologic variability may be linked to genomic instability, dysregulated cell cycling, and epigenetic modifications that promote clonal evolution under therapeutic pressure [28, 29]. Textural disorganization, on the other hand, may reflect stromal activation, immune exclusion, or vascular abnormalities that compromise drug delivery and efficacy [19, 20]. The strong performance of NHP suggests that it serves as a surrogate for the overall mutational and phenotypic diversity within the tumor, which has been shown by Wang et al. [30] to influence therapeutic responses in ccRCC. Moreover, the presence of

cancer stem cells (CSCs) and EMT-like transitions, as described by La Fleur et al. [31], may contribute to both the morphologic heterogeneity observed in pathomics and the development of resistance.

Despite these promising findings, several limitations of this study should be acknowledged. The retrospective design introduced potential biases in patient selection and data collection. Although external validation was performed, the sample size of the test cohort was relatively small, and future studies with larger, multi-center cohorts are needed to further verify the model's robustness. In addition, we did not perform formal subgroup analyses stratified by TNM stage, Fuhrman grade, or specific VEGFR-TKI agent (sunitinib vs. pazopanib), nor did we test for statistical interactions between pathomics features and clinical variables. These analyses were precluded by limited statistical power within subgroups and the risk of overfitting; however, they represent important next steps to determine whether the model's predictive performance varies across patient populations or treatment contexts. Future studies with larger, more diverse cohorts should systematically evaluate model performance in predefined subgroups and explore potential effect modification by clinical and pathologic characteristics. It should be noted that the external validation AUC (0.925) exceeded the training AUC (0.888), which, while unusual, can occur when the test cohort has a narrower case-mix spectrum or when the training cohort exhibits greater outcome heterogeneity, as previously described in methodological literature [32]. Importantly, the locked model was applied without any refitting, and the high validation performance likely reflects the robustness of the extracted pathomics features; however, this finding warrants confirmation in larger, more diverse populations. It should be noted, however, that the training cohort satisfied the recommended EPV criterion (162 events for 12 predictors, EPV=13.5), supporting the internal validity of the model development process. Additionally, our definition of resistance combined both primary and early acquired resistance. While this endpoint is clinically pragmatic for predicting first-line treatment failure, these two entities may have distinct biological drivers [16, 18]. Future investigations with larger patient populations should aim to stratify these resistance phenotypes to enable more granular mechanistic insights and tailored therapeutic approaches. Additionally, the pathomics features were extracted from two-dimensional H&E images, which may not fully capture the three-dimensional spatial architecture of tumors or the heterogeneity across deeper tissue layers. The definition of resistance was based on radiological progression within 12 months, which, while clinically relevant, may not account for later-onset resistance or the influence of subsequent therapy lines.

Future research should focus on prospective validation of the model in randomized clinical trial settings to assess its impact on therapeutic decision-making and patient outcomes. Integration of additional data layers, such as genomic, transcriptomic, or proteomic profiles, could further enhance the model's predictive power and provide deeper insight into the biological mechanisms linking heterogeneity to resistance. Moreover, the application of more advanced deep learning techniques, including attention-based models and spatial transcriptomics, may allow for even more precise mapping of intratumoral heterogeneity and its functional consequences.

Conclusion

We established a pathomics-based framework for predicting drug resistance in ccRCC that effectively combines quantitative histologic heterogeneity with clinical risk factors. The model demonstrated strong performance and generalizability, highlighting the potential of computational pathology to extract actionable insights from standard medical images. By capturing the biological complexity of tumor heterogeneity, this approach offers a promising step toward more personalized and effective management of ccRCC.

Acknowledgements

This study was supported by the Research Project of Heilongjiang Provincial Health Commission (No. 20240404050417).

Disclosure of conflict of interest

None.

Address correspondence to: Guangchi Xu, Department of Urology, The Second Affiliated Hospital of Qiqihar Medical University, 64 Zhonghua West

Road, Jianhua District, Qiqihar 161006, Heilongjiang, China. E-mail: Oyxuguangchi@163.com

References

[1] Zou S, Cui L, Pai P, Lu Y, Li X, Wang G, Huang W, Wang D, Shaikh N, Peng Z, Peng Z, He H and Liao Z. Incidence and survival patterns of clear cell renal cell carcinoma from 2000 to 2017: a seer database analysis. J Cancer 2025; 16: 1591-1597.

[2] Yang J, Wang K and Yang Z. Treatment strategies for clear cell renal cell carcinoma: past, present and future. Front Oncol 2023; 13: 1133832.

[3] Yue X, Yang C, Cao D and Li Y. Niraparib for the treatment of metastatic ccRCC in a patient with CDK12 and RAD51C mutations: a case report. Front Pharmacol 2024; 15: 1396606.

[4] Bielecka ZF, Czarnecka AM, Solarek W, Kornakiewicz A and Szczylik C. Mechanisms of acquired resistance to tyrosine kinase inhibitors in clear - cell renal cell carcinoma (ccRCC). Curr Signal Transduct Ther 2014; 8: 218-228.

[5] Peng S, Xie Z, Jiang H, Zhang G and Chen N. Revealing the characteristics of SETD2-mutated clear cell renal cell carcinoma through tumor heterogeneity analysis. Front Genet 2024; 15: 1447139.

[6] Zheng J, Lu W, Wang C, Chen S, Zhang Q and Su C. Unfolding the mysteries of heterogeneity from a high-resolution perspective: integration analysis of single-cell multi-omics and spatial omics revealed functionally heterogeneous cancer cells in ccRCC. Aging (Albany NY) 2024; 16: 10943-10971.

[7] Li QK, Pavlovich CP, Zhang H, Kinsinger CR and Chan DW. Challenges and opportunities in the proteomic characterization of clear cell renal cell carcinoma (ccRCC): a critical step towards the personalized care of renal cancers. Semin Cancer Biol 2019; 55: 8-15.

[8] Ferronika P, Kats-Ugurlu G, Haryana SM, Utoro T, Rinonce HT, Danarto R, de Lange K, Terpstra MM, Sijmons RH, Westers H and Kok K. Mutational heterogeneity between different regional tumour grades of clear cell renal cell carcinoma. Exp Mol Pathol 2020; 115: 104431.

[9] Raufaste-Cazavieille V, Santiago R and Droit A. Multi-omics analysis: paving the path toward achieving precision medicine in cancer treatment and immuno-oncology. Front Mol Biosci 2022; 9: 962743.

[10] Kwon YW, Jo HS, Bae S, Seo Y, Song P, Song M and Yoon JH. Application of proteomics in cancer: recent trends and approaches for biomarkers discovery. Front Med (Lausanne) 2021; 8: 747333.

[11] Lee JH, Song GY, Lee J, Kang SR, Moon KM, Choi YD, Shen J, Noh MG and Yang DH. Prediction of immunochemotherapy response for diffuse large B-cell lymphoma using artificial intelligence digital pathology. J Pathol Clin Res 2024; 10: e12370.

[12] Murchan P, Ó'Brien C, O'Connell S, McNevin CS, Baird AM, Sheils O, Ó Broin P and Finn SP. Deep learning of histopathological features for the prediction of tumour molecular genetics. Diagnostics (Basel) 2021; 11: 1406.

[13] Matos I, Martin-Liberal J, García-Ruiz A, Hierro C, Ochoa de Olza M, Viaplana C, Azaro A, Vieito M, Braña I, Mur G, Ros J, Mateos J, Villacampa G, Berché R, Oliveira M, Alsina M, Elez E, Oaknin A, Muñoz-Couselo E, Carles J, Felip E, Rodón J, Tabernero J, Dienstmann R, Perez-Lopez R and Garralda E. Capturing hyperprogressive disease with immune-checkpoint inhibitors using RECIST 1.1 criteria. Clin Cancer Res 2020; 26: 1846-1855.

[14] Damodaran K, Crestani M, Jokhun DS and Shivashankar GV. Nuclear morphometrics and chromatin condensation patterns as disease biomarkers using a mobile microscope. PLoS One 2019; 14: e0218757.

[15] Mariean CR, Tiucă OM, Mariean A and Cotoi OS. Cancer cachexia: new insights and future directions. Cancers (Basel) 2023; 15: 5590.

[16] Xiang Y, Zheng G, Zhong J, Sheng J and Qin H. Advances in renal cell carcinoma drug resistance models. Front Oncol 2022; 12: 870396.

[17] Gerlinger M, Rowan AJ, Horswell S, Math M, Larkin J, Endesfelder D, Gronroos E, Martinez P, Matthews N, Stewart A, Tarpey P, Varela I, Phillimore B, Begum S, McDonald NQ, Butler A, Jones D, Raine K, Latimer C, Santos CR, Nohadani M, Eklund AC, Spencer-Dene B, Clark G, Pickering L, Stamp G, Gore M, Szallasi Z, Downward J, Futreal PA and Swanton C. Intratumor heterogeneity and branched evolution revealed by multiregion sequencing. N Engl J Med 2012; 366: 883-892.

[18] Sweeney PL, Suri Y, Basu A, Koshkin VS and Desai A. Mechanisms of tyrosine kinase inhibitor resistance in renal cell carcinoma. Cancer Drug Resist 2023; 6: 858-873.

[19] Fumadó Navarro J and Lomora M. Mechanoresponsive drug delivery systems for vascular diseases. Macromol Biosci 2023; 23: e2200466.

[20] Borlongan MC, Saha D and Wang H. Tumor microenvironment: a niche for cancer stem cell immunotherapy. Stem Cell Rev Rep 2024; 20: 3-24.

[21] Zhang A, Miao K, Sun H and Deng CX. Tumor heterogeneity reshapes the tumor microenvironment to influence drug resistance. Int J Biol Sci 2022; 18: 3019-3033.

[22] Yuan J, Zhang Y and Wang X. Application of machine learning in the management of lymphoma: current practice and future prospects. Digit Health 2024; 10: 20552076241247963.
[23] Prabhu S, Prasad K, Robels-Kelly A and Lu X. AI-based carcinoma detection and classification using histopathological images: a systematic review. Comput Biol Med 2022; 142: 105209.
[24] Bhat GR, Sethi I, Sadida HQ, Rah B, Mir R, Algehainy N, Albalawi IA, Masoodi T, Subbaraj GK, Jamal F, Singh M, Kumar R, Macha MA, Uddin S, Akil ASA, Haris M and Bhat AA. Cancer cell plasticity: from cellular, molecular, and genetic mechanisms to tumor heterogeneity and drug resistance. Cancer Metastasis Rev 2024; 43: 197-228.
[25] Coppo R and Inoue M. Patient-derived tumor organoids to model cancer cell plasticity and overcome therapeutic resistance. Cells 2025; 14: 1464.
[26] Ghorbian S. Cancer cell plasticity and therapeutic resistance: mechanisms, crosstalk, and translational perspectives. Hereditas 2025; 162: 188.
[27] Steyerberg EW, Vickers AJ, Cook NR, Gerds T, Gonen M, Obuchowski N, Pencina MJ and Kattan MW. Assessing the performance of prediction models: a framework for traditional and novel measures. Epidemiology 2010; 21: 128-138.
[28] Tuo Z, Zhang Y, Li D, Wang Y, Wu R, Wang J, Yu Q, Ye L, Shao F, Wusiman D, Yang Y, Yoo KH, Ke M, Okoli UA, Cho WC, Heavey S, Wei W and Feng D. Relationship between clonal evolution and drug resistance in bladder cancer: a genomic research review. Pharmacol Res 2024; 206: 107302.
[29] Fatma H and Siddique HR. Cancer cell plasticity, stem cell factors, and therapy resistance: how are they linked? Cancer Metastasis Rev 2024; 43: 423-440.
[30] Wang J, Zuo Z, Yu Z, Chen Z, Meng X, Ma Z, Niu J, Guo R, Tran LJ, Zhang J, Jiang T, Ye F, Ma B and Sun Z. Single-cell transcriptome analysis revealing the intratumoral heterogeneity of ccRCC and validation of MT2A in pathogenesis. Funct Integr Genomics 2023; 23: 300.
[31] La Fleur L, Johansson AC and Roberg K. A CD-44high/EGFRlow subpopulation within head and neck cancer cell lines shows an epithelial-mesenchymal transition phenotype and resistance to treatment. PLoS One 2012; 7: e44071.
[32] Vergouwe Y, Moons KG and Steyerberg EW. External validity of risk models: use of benchmark values to disentangle a case-mix effect from incorrect coefficients. Am J Epidemiol 2010; 172: 971-980.